Aluminium segregation profiles in the (110), (100) and (111) surface regions of the Fe 0.85 Al 0.15 random body-centered cubic alloy

Zongbei Dai, Patrizia Borghetti, Stéphane Chenot, Pascal David, Alexey Koltsov, Jacques Jupille, Gregory Cabailh, Jacek Goniakowski, Rémi Lazzari

HAL Id: hal-02340100

https://hal.sorbonne-universite.fr/hal-02340100

Submitted on 30 Oct 2019

Aluminium segregation profiles in the (110), (100) and (111) surface regions of the $Fe_{0.85}Al_{0.15}$ random body-centered cubic alloy

Zongbei Dai[1], Patrizia Borghetti[1], Stéphane Chenot[1], Pascal David[1], Alexey Koltsov[b], Jacques Jupille[1], Gregory Cabailh[1], Jacek Goniakowski[1], Rémi Lazzari[1,*]

[a]*CNRS, Sorbonne Universités, Institut des NanoSciences de Paris, UMR 7588, 4 Place Jussieu, F-75005 Paris, France*
[b]*ArcelorMittal Maizieres Research, voie Romaine, F-57280, Maizières-lès-Metz, France*

Abstract

Thanks to a dedicated modelling of intensities, the depth sensitivity of X-ray photoemission is used to probe the segregation profile of aluminium at the (110), (100) and (111) low index surfaces of the body-centred $Fe_{0.85}Al_{0.15}$ random alloy. Sputtered surface composition is close to the nominal bulk one, thus excluding preferential sputtering. Surface enrichment in aluminium upon annealing starts at around 700 K before reaching a stationary state above 1000 K. The average surface composition is close to $Fe_{0.5}Al_{0.5}$, corresponding to the B_2 CsCl structure on the phase diagram. The impacted depth, that is in the range of 2.5-3.5 nm, is quite significant. Although not evidenced previously in surface science conditions at FeAl single crystal surfaces, it is qualitatively in agreement with the segregation at grain boundaries and shear planes of Al-alloyed steels. This segregation tendency is rationalized through *ab initio* calculations.

Keywords: iron aluminide, segregation, random alloy

*Corresponding author
Email address: remi.lazzari@insp.jussieu.fr (Rémi Lazzari)

1. Introduction

FeAl-based alloys are very promising light-weight metallic materials that combine high strength and corrosion resistance at high temperature [1, 2, 3, 4]. A particular case of application is encountered in the Advanced High Strengh Steels (AHSS) involving high concentrations of alloying elements such as aluminium. Those grades are developed by the steel industry to face the challenge of reducing CO_2 emission from cars by decreasing their weight while keeping intact mechanical properties of steel sheets at an affordable price. Aluminium alloying, which of course lightens the steel, has the additional advantage of improving the elasticity limit and the stiffness (elasticity limit/density ratio) performance of the material [4, 5, 6, 7, 8, 9]. The subject thus relates to other scopes of application, in particular the aircraft industry. Very effective in improving the mechanical properties of steel, the added aluminium has adverse effects, including the formation of brittle compounds that reduce ductility (Ref. [4] and references therein) and the oxygen-induced segregation of alumina at the steel surface, degrading the quality of the anti-corrosion zinc coating, commonly referred to as galvanization [10, 11, 12, 13, 14, 15, 16]. To be more specific, despite a reducing atmosphere that prevents iron oxidation, segregation occurs during the recrystallization annealing of the Al-alloyed steel at 1070 K, which is the last production stage of steel sheets prior to galvanization [10, 11, 12, 14, 15, 16].) Indeed, the formation of both surface alumina films [13] and brittle compounds [4, 17, 18] originates from the aluminium segregation at either the surface or the grain boudaries and shear bands. Therefore, the knowledge of the segregation at the Al-alloyed steel surface and interfaces is a prerequisite for the understanding of both the behavior in oxidizing environment and the mechanical properties of the material. Faced with the complexity of the various steel compositions, binary FeAl alloys are often used as model systems to mimic the behavior of Al-alloyed steels [9, 4]. An approach of this type is undertaken herein. Indeed, although segregation equilibria at interfaces compare to those at surfaces, the latter are easier to study. An additional advantage is the possibility of analysing the dependence on crystallographic orientations. The present work focuses on the aluminium segregation at the $Fe_{0.85}Al_{0.15}$ surface vacuum interface as a function of the surface orientation, *i.e.* (100), (110) and (111). This composition has been chosen because of its structural similarity with the Al-alloyed steel. In the Fe-Al phase diagram [19, 20, 21, 22, 23, 24] (Fig. 1), at increasing Al content, a body-centred

cubic (bcc) random alloy phase (Strukturbericht symbol A_2) appears first, followed by ordered phases of B_2 (CsCl structure) and $D0_3$ type, and by a series of more complex Fe-rich intermetallic coumpounds [22, 25, 19, 20]. The effect of crystal orientation on segregation is tackled herein on the representative $Fe_{0.85}Al_{0.15}$ composition which is stable and adopts the ferritic A_2 solid solution up to its melting temperature. According to the Fe-Al-C phase diagram [24], the incorporation of carbon in actual steel grades introduces the well-known austenite (bcc) to ferrite (face-cubic centred) transition at high temperatures. The transition shifts down in temperature with carbon content and up with Al content in $Fe_{1-x}Al_x$. But with a 5-at% of C, the transition temperature around 1173 K for $Fe_{0.85}Al_{0.15}$ is above the recrystallization annealing temperature of alloyed steel sheets. Regarding industrially relevant Fe-Al-Mn-C grades [26], the micro structure is even more complex. But, in general, the recrystallization annealing in reducing atmosphere induces a decarburization of superficial layers which stabilizes the ferrite bcc phase over micrometer length scales. Therefore, the bcc $Fe_{0.85}Al_{0.15}$ used herein may be a good model system to mimic Al-segregation phenomena in many alloyed steel grades.

Surface segregation is one of the driving forces of reconstruction on both ordered and disordered metallic alloys [27, 28, 29]. It consists in an enrichment with a given constituent through diffusion in the vicinity of a surface. For ordered alloys, such an effect can produce new ordered phases or some disordered antisite phase with respect to the bulk. Regarding random alloys with substitutional disorder, the variable concentration of enriched element found in near surface layers draws the so-called segregation profile, which may be oscillatory, before converging towards the bulk concentration [30]. The commonly accepted driving forces of surface segregation are (i) the reduction of the surface free energy, (ii) the reduction of surface stress due to differences in atomic sizes between solvent and solute; (iii) the decrease of the elemental heat of vaporization reflected in a broken bond approach by the bond strength of the elements under consideration. The Al heat of vaporization and surface free energy for all orientations are weaker than that of Fe (284 kJ.mol^{-1} vs 354 kJ.mol^{-1} for the heat of vaporization [31] and about a factor two for either experimental or theoretical values of the (100), (110) and (111) surface energies [32, 33, 34]). In line with the above rules, those data are consistent with the constant observation upon annealing that all surface orientations of $Fe_{1-x}Al_x$ are characterized by Al surface segregation on either single crystal [35, 36, 37, 30, 25, 38, 39] or polycrystalline surfaces [40]. Enrichment in
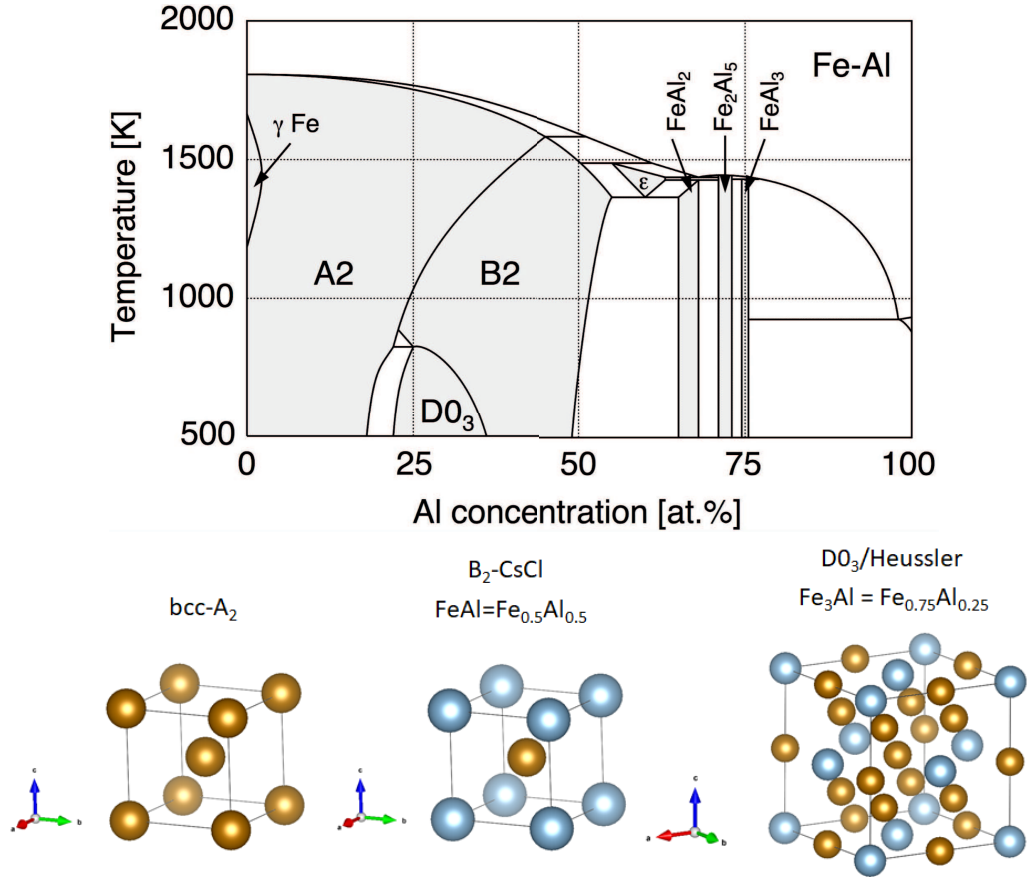
3

Figure 1: Fe-Al binary phase diagram where the most important compounds (shaded area) are labelled by their Strukturbericht symbol and/or their formula. The corresponding ball models are shown below (Fe in brown and Al in light blue). Interpreted from Ref. [21].

Al of the deeper layers is also observed [37, 25], in particular in the case of the more opened surfaces in which a multilayer segregation of Al occurs [37]. The onset of the phenomenon is around 600-800 K [35, 36, 37, 25, 38, 40] and depends on bulk composition. Upon annealing, the Al segregation onset is observed at 623 K on the ordered B_2-$Fe_{0.53}Al_{0.47}(100)$ surface [35, 37, 41]. At 683 K, the surface average composition is $Fe_{0.38}Al_{0.62}$ with a pure Al termination [41, 42]. Above 1100 K, the $Fe_{0.85}Al_{0.15}(100)$ surface Al concentration is beyond half a monolayer [25, 38]. It can reach up to 75 % as derived from low energy ion scattering data [43]. The oscillatory behavior of the composition suggested to occur on all $Fe_{1-x}Al_x(100)$ surfaces [36, 25] was assigned to favorable nearest-neighbours interactions [25]. Several studies of the B_2 FeAl(110) orientation have been reported [35, 37, 30, 39, 44, 45, 46]. Annealing at 673 K the sputtered Al-depleted surface of $Fe_{0.53}Al_{0.47}(110)$ results in Al segregation. The stoichiometry of the superstructure is close to $FeAl_2$ with an estimated Al concentration in the last plane of 0.67 according to Auger spectroscopy [44] and X-ray diffraction (XRD) results [35, 37]. The more open FeAl (111), (211) and (310) surfaces were studied only in Ref. [37]. Upon annealing the FeAl(111) orientation, the surface Al concentration increases continuously and almost linearly with temperature in contrast to the other orientations of the alloy. This proves severe multilayer Al segregation which again can be explained by the specific bcc(111) open structure. However, it should be noticed that the corrugated amplitude of the FeAl(111) surface is comparable with the escape depth of Auger electrons increasing the uncertainty in the determination of near-surface concentration on which these conclusions are based [37].

Such behaviors are in stark contrast with the nearly bulk-terminated NiAl alloy surfaces. If the large surface energy and heat of vaporization of transition metals compared to Al favors segregation, it can be counterbalanced by a large (absolute) heat of formation of the alloy. The larger this quantity, the less favorable the interchange of constituents. The respective heats of formation ($\Delta H(FeAl) = -25.1$ kJ.mol$^-$1, $\Delta H(Fe_3Al) = -13.0$ kJ.mol$^-$1, $\Delta H(NiAl) = -58.9$ kJ.mol$^-$1, $\Delta(CoAl) = -54.2$ kJ.mol$^-$1) explain why FeAl alloys are prone to Al segregation while NiAl and CoAl are not [37] and (ii) why NiAl alloy surfaces are nearly bulk terminated. Moreover, ordering tendency in the alloy will hamper segregation since the latter favors the occupation of neighbouring lattice sites by the same atomic species while ordering causes exactly the opposite [29].

Of relevance as a model for Al-alloyed steel, the $Fe_{0.85}Al_{0.15}$ random alloy is poorly explored in the FeAl literature which deals mainly with the B_2 ordered compound [42, 35, 41, 39]. However, this alloy offers an extra degree of freedom related to the gradient of composition. The interplay between segregation, crystal structure, long- and short-range order is quite complex (see review Refs. [27, 28, 29]). The status of the surface segregation may be affected by the sample preparation mode. In particular, preferential sputtering may induce an artificial enrichment in one of the elements since ion bombardment is a mandatory step in the preparation of a clean surface. Some authors [35, 37, 30, 25, 47, 41, 38, 39] claimed preferential sputtering of Al leading to a depletion in Al at the surface without clear proof. But, estimates of the sputtering yield [48, 49] for a Fe target (1.7 atom/ion) and of an Al one (1.53 atom/ion) with 1 keV Ar^+ ion would slightly favor preferential Fe sputtering as observed herein. Finally, in such alloys, the segregation process concerns not only the extreme surface as often determined by low-energy electron diffraction but also subsurface layers [35, 41, 39].

Therefore, a particular attention is paid herein to the evolution of the concentration throughout the depth probed by photoelectron spectroscopy. Modeling of the photoemission signal angular dependence is developed (Sect. 2.3-3) to determine the segregation profile (Sect. 3). A particular effort was made to address the underlying question of the actual equilibrium between bulk and (sub)surface concentrations [36, 50]. The reproducibility of the surface composition after sputtering/annealing was checked through intensity ratios of photoemission peaks. *Ab initio* calculations were used to rationalize some observed trends (Sect. 4). The associated surface structures studied by low energy electron diffraction, grazing incidence x-ray scattering and scanning tunnelling microscopy will be addressed in a forthcoming paper.

2. Methods

2.1. Structural aspects of $Fe_{0.85}Al_{0.15}$ surfaces

The A_2 bulk truncation along the (100), (110) and (111) low index orientations are shown in Fig. 2. While all atoms are coplanar on the (100) and (110) faces (Fig. 2-a,b), the (111) surface is opened and atomically rough; it involves three atomic planes which define a physical monolayer (Fig. 2-c). If $a_B = 2.89$ Å is the bulk cubic lattice parameter, the distance between atomic planes is $a_B/2 = 1.45$ Å , $a_B/\sqrt{2} = 2.04$ Å , $a_B/2\sqrt{3} = 0.83$ Å for
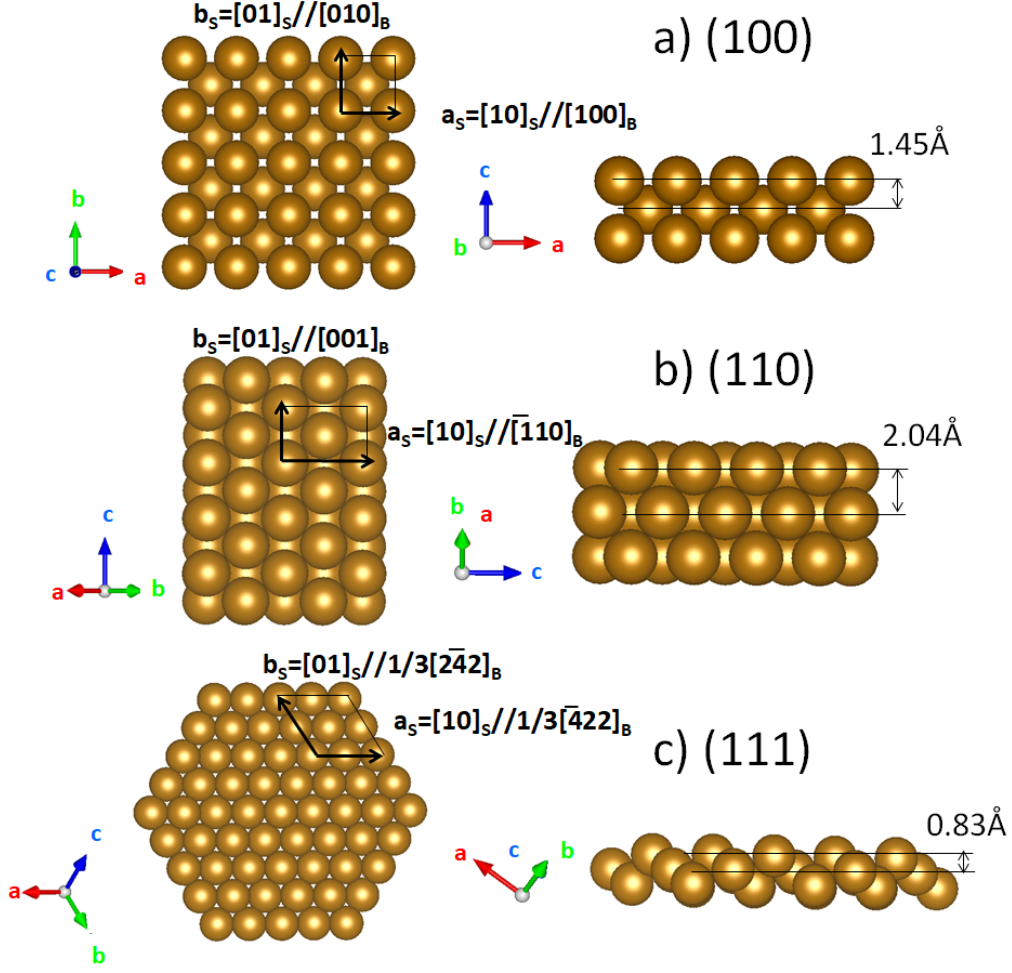
6

Figure 2: Ball models of the a) (100), b) (110) and c) (111) faces of the $Fe_{0.85}Al_{0.15}$ bcc A_2 random alloy ($a_B = 2.89$ Å [51]). The bulk cubic unit cell vectors $(\mathbf{a}_B, \mathbf{b}_B, \mathbf{c}_B)$ are shown with coloured arrows while black arrows are the surface ones $(\mathbf{a}_S, \mathbf{b}_S)$. Left column: top view along a) $[010]_B$, b) $[110]_B$, c) $[111]_B$. Right column: side view along a) $[010]_B$, b) $[1\bar{1}0]_B$, c) $[1\bar{1}0]_B$. Monolayer heights are indicated on the right.

the $(100), (110)$ and (111) faces, respectively. The atomic density per unit of surface is given by: $n_S = 1/a_B^2$, $n_S = \sqrt{2}/a_B^2$, $n_S = 3\sqrt{3}/4a_B^2$ for $(100), (110)$ and (111) faces leading to the hierarchy $n_S(100) < n_S(111) < n_S(110)$. This coverage will be used to define the monolayer for each orientation; this corresponds to 1.2×10^{15} atom.cm^{-2} on (100), 1.55×10^{15} atom.cm^{-2} on (111) and 1.69×10^{15} atom.cm^{-2} on (110).

2.2. Experimental setups

Aluminium segregation at $Fe_{0.85}Al_{0.15}$ surfaces was studied by (i) X-ray Photoemission Spectroscopy (XPS) under non-monochromatic Mg/Al-Kα excitation with an hemispherical analyzer (Omicron EA-125, 5 channeltrons), (ii) Low-Energy Electron Diffraction (LEED) and (iii) Scanning Tunneling Microscopy (STM, Omicron). Experiments were performed in two connected ultra-high vacuum (UHV) chambers (preparation and analysis) with base pressures of 3×10^{-10} and 5×10^{-11} mbar, respectively. The $Fe_{0.85}Al_{0.15}$ single crystals [52] ($\Phi = 6$ mm, thickness 2 mm, lattice parameters 2.8914 Å [51]) cut along (100), (110) and (111) low index orientations within $0.1°$ were mounted on a Ta plate by spot-welding with wires inserted in a groove machined in the crystal edges. Samples were annealed by electron bombardment of the Ta backplate. Surfaces were prepared by cycles of Ar$^+$ sputtering (1 keV, incidence $45°$, current $\sim 10~\mu A$) for 20-45 minutes at room temperature followed by annealing. The annealing duration for each plateau values in the 673-1273 K temperature range was kept fixed (15 min) while heating/cooling was performed as fast as possible (~ 250 K.min^{-1}) to quench the resulting concentration profile. Temperature was measured by optical pyrometry with an emissivity previously calibrated on a thermocouple. The annealing temperature was kept below 1300 K to avoid Al evaporation [35, 36]. Bulk contaminants were below the detection level, except on the (110) surface for which a temporary carbon segregation in the form self-organized stripes was observed [53, 54]. Fortunately, after several cycles of preparation, a carbon free surface could be obtained. Due to the high reactivity of aluminium, special care was taken to minimize contamination due to residual background, the Al 2p core level being a good indicator of the associated oxidation phenomenon [53]. Reproducible surface reconstruction and topography could be obtained on all surfaces; results will be presented elsewhere.
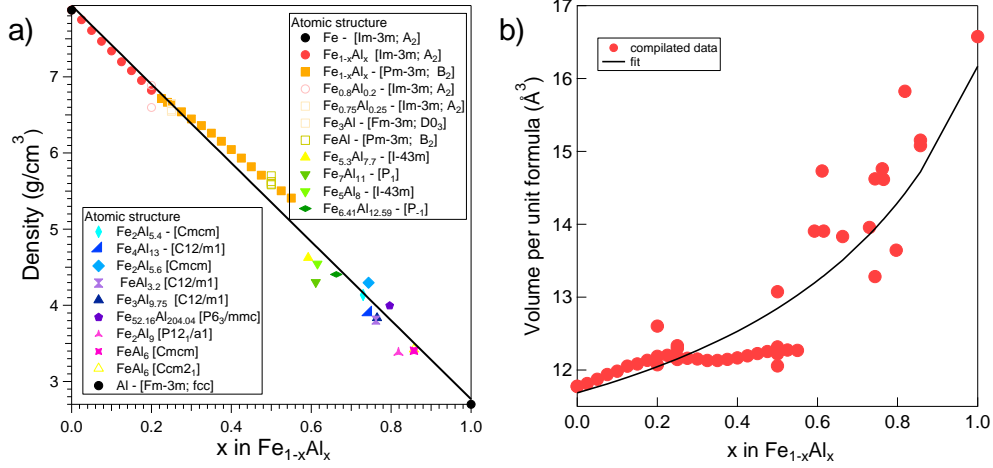
8

2.3. The inelastic mean free in the alloy

Figure 3: a) Compilation of the density $\rho(x)$ of all the $Fe_{1-x}Al_x$ compounds tabulated in the ICSD database overlapped with the measurements of Ref. [51] for the A_2 (red filled circles) and B_2 (orange filled squares) structures. The legend gives the corresponding compounds as well as their space groups. Data are well accounted for by a linear regression (black line). b) Corresponding hyperbolic variation of the atomic volume.

   The analysis of the segregation profile by photoemission requires the knowledge of the inelastic mean free path $\lambda(x)$ in $Fe_{1-x}Al_x$. Sizeable variations are expected as a function of x since $\lambda(x = 0)$ in bulk Fe (A_2 bcc) strongly differs from $\lambda(x = 1)$ in bulk Al (A_1 fcc) [55]. At any kinetic energy, the difference in electronic density between aluminium (0.18 e.$Å^{-3}$) and iron (1.35 e.$Å^{-3}$) results in a difference up to 10 Å between the two materials. $\lambda(x)$ was estimated with the TPP-2M predictive formula of Tanumma, Powell and Penn [56, 55, 57, 58, 59, 60, 61, 62, 63]. The ingredients used in the QUASES-IMFP-TPP2M software [64] were the bulk density $\rho(x)$, the molar mass $M(x) = (1 - x)M_{Fe} + xM_{Al}$ with $M_{Fe} = 55.85$ g.mol^{-1} and $M_{Al} = 26.98$ g.mol^{-1}, a gap-less material and the total number of valence electrons of binding energy below 30 eV. The latter was given by a linear interpolation of the electronic structure of Fe ([Ne] $3s^2$ $3p^6$ $4s^2$ $3d^6$) and of Al ([Ne] $3s^2$ $3p^1$) accordingly to the atomic fraction x. More precisely, the electron distribution per unit formula between d and s+p orbitals of low and high binding energies were taken as $6(1-x)$, $8(1-x)$ and $x+2$, respectively,

9

giving a total number of electrons of $-13x + 16$. Regarding the bulk density $\rho(x)$, a careful analysis of all the Fe-Al compounds reported in the Inorganic Crystal Structure Database (ICDS [65]) was undertaken including (i) the A_2-bcc and A_1-fcc structures of pure Fe and Al, (ii) the most interesting data for A_2-bcc random alloy and for the high temperature quenched ordered B_2-CsCl alloys [51], (iii) the ordered Heussler $D0_3$ alloys (Fe_3Al) and (iv) more exotic high temperature compounds of various symmetries in the Al rich zone of the phase diagram. The gathered data (Fig. 3-a) show a change from 2.7 g.cm^{-3} (Al, $x = 1$) up to 7.86 g.cm^{-3} (Fe, $x = 0$) that follows a robust linear dependence $\rho(x) = 7.94 - 5.17x$ g.cm^{-3} corresponding to a hyperbolic variation of the volume per atom $V(x) \sim \rho(x)/M(x)$ or of the atomic concentration $n(x) \sim M(x)/\rho(x)$ (Fig. 3-b). These dependencies will be assumed to hold even at segregated surfaces since they include numerous local environments of Fe and Al.

The obtained TPP-2M inelastic mean free paths $\lambda(x)$ are plotted in Fig. 4 for the most intense core levels of the alloy at the usual Al-Kα (Fig. 4-a) and Mg-Kα (Fig. 4-b) excitation energies. Up to a molar fraction of $x \simeq 0.8$, the variation of $\lambda(x)$ is more moderate than expected from pure Fe and Al. Nevertheless, it was accounted for in the following analysis through a polynomial fit (lines in Fig. 4). Finally, one should keep in mind that the accuracy of the TPP-2M formula is about 20 % [56, 55, 57, 58, 59, 60, 61, 62, 63].

2.4. Photoemission modelling of the segregation

At the opposite of a film on a substrate, the complexity of segregation lies in the absence of bulk reference. Once corrected for the analyzer transmission function T and the photo-ionization cross section σ, ratios of background-subtracted core level intensities can trace back concentration profiles $x(z)$ through the exponential damping of the signal with depth z. Three models have been used herein, namely the homogeneous alloy, the segregated layer and the continuous segregation profile.

Bulk alloy. If an element A is homogeneously mixed with an element B in a solid solution $A_{1-x}B_x$ (Fig. 5-a), atomic concentrations are given by $n_A \sim 1 - x$ and $n_B \sim x$. The atomic ratio x can be determined from the measured
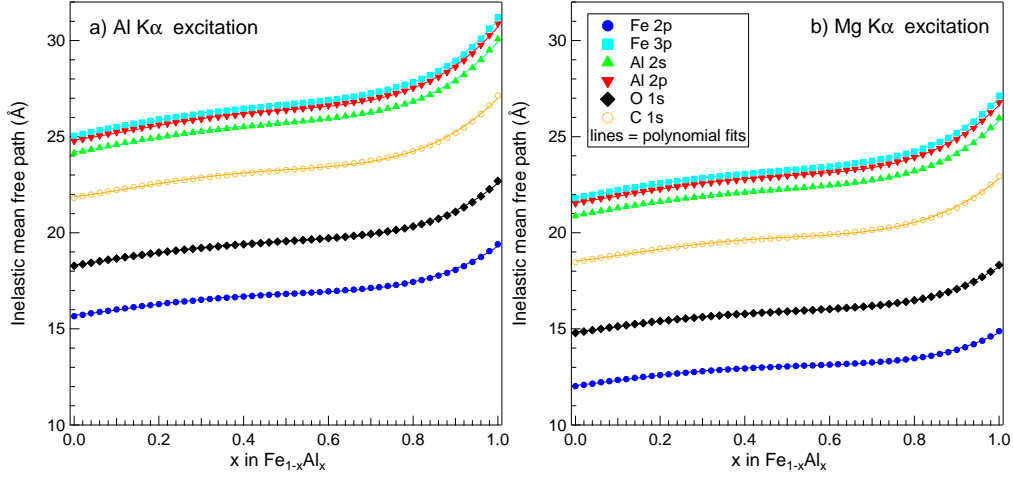
Figure 4: TPP-2M calculated inelastic mean free paths of $Fe_{1-x}Al_x$ compounds at the kinetic energies of Fe 2p, Fe 3p, Al 2s, Al 2p, O 1s and C 1s for a) Al-Kα ($h\nu = 1486.6$ eV) and b) Mg-Kα ($h\nu = 1253.6$ eV) photon excitations (see text).
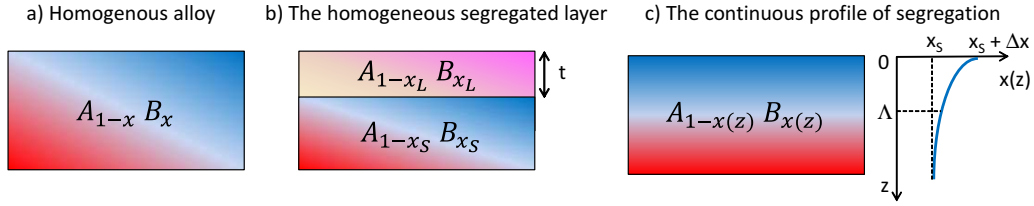

Figure 5: Concentration profile models used for photoemission analysis. a) The homogeneous semi-infinite alloy $A_{1-x}B_x$. b) The homogeneous segregated layer $A_{1-x_L}B_{x_L}$ on a semi-infinite alloy $A_{1-x_S}B_{x_S}$. c) The continuous segregation profile $A_{1-x(z)}B_{x(z)}$.

intensities I_A and I_B of the given core levels:

$$\frac{I_B}{I_A}\frac{T_A\sigma_A}{T_B\sigma_B} = \frac{x}{1-x}\frac{\lambda_B^{AB}}{\lambda_A^{AB}}, \tag{1}$$

where T_i $(i = A, B)$ is the analyzer transmission function at the corresponding electron kinetic energy, σ_i the photo-ionization cross-section of the core level under consideration and λ_i^{AB} the inelastic mean free path of the photoelectrons from atom i in $A_{1-x}B_x$. The formula is independent of the emission angle Θ between the sample normal and the axis of the analyzer.

The homogeneous segregated layer on a homogeneous alloy. Let's consider a segregated layer $A_{1-x_L}B_{x_L}$ on top of a semi-infinite substrate $A_{1-x_S}B_{x_S}$ (Fig. 5-b). If n_i^j and λ_i^j are the atomic concentrations and mean free paths of element $i = A, B$ in medium $j = L, S$, the photoelectron signals from elements A, B include contributions from the substrate and the layer and read:

$$\begin{aligned}
\frac{I_A}{T_A\sigma_A} &\sim \lambda_A^S n_A^S \exp\left(-t/\lambda_A^L\cos\Theta\right) \\
&+ \lambda_A^L n_A^L\left[1 - \exp\left(-t/\lambda_A^L\cos\Theta\right)\right] \\
\frac{I_B}{T_B\sigma_B} &\sim \lambda_B^S n_B^S \exp\left(-t/\lambda_B^L\cos\Theta\right) \\
&+ \lambda_B^L n_B^L\left[1 - \exp\left(-t/\lambda_B^L\cos\Theta\right)\right]. \tag{2}
\end{aligned}$$

If $V(x)$ is the atomic volume at atomic fraction x, $n_A^S = (1 - x_S)/V(x_S)$, $n_B^S = x_S/V(x_S)$, $n_A^L = (1 - x_L)/V(x_L)$, $n_B^L = x_L/V(x_L)$. With an inelastic mean free path that depends only on the atomic fraction x, the ratio of measured intensities is given by:

$$\frac{I_B}{I_A}\frac{T_A\sigma_A}{T_B\sigma_B} = \frac{\lambda_B(x_S)x_SV(x_L)\exp\left[-\frac{t}{\lambda_B(x_L)\cos\Theta}\right] + \lambda_B(x_L)x_LV(x_S)\left\{1 - \exp\left[-\frac{t}{\lambda_B(x_L)\cos\Theta}\right]\right\}}{\lambda_A(x_S)(1 - x_S)V(x_L)\exp\left[-\frac{t}{\lambda_A(x_L)\cos\Theta}\right] + \lambda_A(x_S)(1 - x_L)V(x_S)\left\{1 - \exp\left[-\frac{t}{\lambda_A(x_L)\cos\Theta}\right]\right\}} \tag{3}$$

From the knowledge of the substrate composition x_S, the previous equation can be used to fit the angular variation of the fraction $\frac{I_B}{I_A}$ to obtain film composition x_L and thickness t.

The continuous profile. The previous model is easily generalized to any continuous profile of atomic fraction $x(z)$ (Fig. 5-d) by integration of the infinitesimal photoelectron signal of layer dz of element i:

$$dI_i \sim T_i \sigma_i n_i(z) \exp\left\{ \int_z^0 dz'/\lambda[x(z')] \cos\Theta \right\} dz. \qquad (4)$$

Using the same hypothesis as above, one obtains:

$$\frac{I_A}{T_A \sigma_A} \sim \int_{-\infty}^0 \frac{1-x(z)}{V[x(z)]} \exp\left\{ \int_z^0 dz'/\lambda_A[x(z')] \cos\Theta \right\} dz$$

$$\frac{I_B}{T_B \sigma_B} \sim \int_{-\infty}^0 \frac{x(z)}{V[x(z)]} \exp\left\{ \int_z^0 dz'/\lambda_B[x(z')] \cos\Theta \right\} dz. \qquad (5)$$

For the sake of simplicity, a diffusion profile has been chosen to analyse the present data:

$$x(z) = x_S + \Delta x \exp(-z^2/\Lambda^2), \qquad (6)$$

where $x_S = 0.15$ is the bulk value, $x_S + \Delta x$ the surface value and Λ a typical segregation length scale.

2.5. Computational methods and settings

Experimental observations have been accompanied by *ab initio* calculations of segregation characteristics of aluminium in iron. All calculations were performed within the Density Functional Theory (DFT) implemented in VASP (Vienna Ab Initio Simulation Package) [66, 67]. The interaction of valence electrons with ionic cores was described within the Projector Augmented Wave (PAW) method [68, 69], and the Kohn-Sham orbitals were developed on a plane-wave basis set with a cutoff energy of 300 eV. Semi-core Fe 3p electrons were treated explicitly. Since the Curie temperature of $Fe_{0.85}Al_{0.15}$ is around 1000 K [23] and samples were found in the ferromagnetic state after thermal treatment, all calculations were spin-polarised with a ferromagnetic ordering of iron spins. Gradient-corrected PW91[70] exchange-correlation functional was used. Positions of all atoms were systematically relaxed until all forces got smaller than 0.01 eV A^{-1}.

For bulk Fe and Al, results summarized in Tab. 1 show a satisfactory agreement between computational and experimental data. A Γ-centred ($10\times10\times10$)

Monkhorst-Pack grid for k-point sampling of the Brillouin zone of the primitive unit cell of bulk iron ($a_B = 2.84$ Å) insures a convergence of the calculated lattice parameters a_B to within 0.005 Å and of the cohesion energy E_{coh} to within 0.005 eV/Fe. A very similar degree of convergence is obtained with an equivalent ($7 \times 7 \times 7$) k-point sampling of the Brillouin zone of bulk aluminium ($a_B = 4.05$ Å) unit cell. Within the simplest energetic model with only nearest neighbour (NN) ϵ_{Al-Al} and ϵ_{Fe-Fe} interactions, the difference of the calculated interaction strengths ($\epsilon_{Fe-Fe} - \epsilon_{Al-Al} = -0.7$ eV) is overestimated with respect to -0.5 eV deduced from experimental cohesive energies. However, since the overestimation of the bulk cohesion energy of Fe is principally due to a less accurate DFT results for an isolated Fe atom, it will not impact directly the calculated segregation profiles.

Fe (bcc)	a_B (Å)	E (eV)	B (GPa)
calc.	2.836	5.06	186
exp.	2.867	4.29	170
Al(fcc)	a_B (Å)	E (eV)	B (GPa)
calc.	4.052	3.43	72
exp.	4.050	3.34	76

Table 1: Calculated and experimental characteristics of bulk iron and aluminium: lattice parameter a_B (Å), cohesion energy E_{coh} (eV), and bulk modulus B (GPa).

The calculated lattice parameters of $Fe_{0.5}Al_{0.5}$ (B_2) and $Fe_{0.75}Al_{0.25}$ ($D0_3$) phases ($a_{B_2} = 2.88$ Å and $a_{D0_3} = 2.87$ Å) are only slightly expanded with respect to pure Fe. The large negative mixing energies calculated with respect to pure bulk aluminium and iron (-0.34 eV and -0.20 eV for B_2 and $D0_3$, respectively), are fully consistent with the existence of the ordered B_2 and $D0_3$ $Fe_{1-x}Al_x$ phases and in agreement with the large thermodynamics literature [21, 71, 72]. Consistently, the corresponding (average) effective NN pair interaction,[73] $V = (\epsilon_{Fe-Fe} + \epsilon_{Al-Al} - 2\epsilon_{Fe-Al})/2$, is positive (preference to form hetero-atomic bonds) and equal to 0.2 eV. Calculations of Al segregation characteristics for different Fe surface orientations were performed in slab geometry. Slabs composed of 9, 11, and 15 atomic layers with bulk Fe lattice parameters have been used to represent (110), (100), and (111) surfaces, respectively. With these settings the Fe surface energies (2.45 J/m^2, 2.53 J/m^2, and 2.67 J/m^2, respectively) converge to within 0.01 J/m^2.

3. Photoemission analysis of the segregation at $Fe_{0.85}Al_{0.15}$ surfaces

On all surfaces, temperature-induced Al segregation was scrutinized by photoemission through the evolution of the core level intensity ratio $I_{Al\,2p}/I_{Fe\,3p}$ corrected from (i) the transmission function of the analyzer $T(E_K) \sim E_K^{-1}$ [74], (ii) the photo-ionization cross sections $\sigma(E_K)$ [75] and (iii) a Shirley background [76]. These lines were selected because the similarity of their binding energies minimize the error due to transmission function in the quantification while the high kinetic energies associated with them maximize the probing depth. Their ratio is poorly sensitive to forward scattering effects along the dense crystallographic directions since, regardless of short range ordering, Al and Fe occupy the same bcc lattice sites. Finally, the probed elements belong only to the substrate and not to the sample holder, an important caution at large take-off angles.

Fig. 6 shows the evolution of $I_{Al\,2p}/I_{Fe\,3p}$, on surfaces cleaned by sputtering, as a function of the annealing temperature. Similar thermal cycles were applied for each annealing temperature. Those *ex situ* data acquired at normal emission $\Theta = 0°$ were compared to *in situ* annealing, *i.e.* performed directly on the analysis chamber manipulator, at increasing temperatures and at grazing emission, $\Theta = 60°$. Data were analysed by giving the material a homogeneous bulk composition $Fe_{1-x}Al_x$ (Eq. 1) to obtain the equivalent atomic fraction x. The error bars come from a cumulative total uncertainty of 20 % on measured intensities and mean free path determination. Contrary to what is commonly accepted [47, 35, 41, 38, 37, 30, 25, 39], a strong surface enrichment due to preferential sputtering is to be excluded since normal and grazing emissions at T=300 K match within the uncertainty of the measurements. An average composition of $x = 0.19 \pm 0.05$ is found for sputtered surfaces, a value close to bulk expectation $x = 0.15$. Estimates of the sputtering yield using the formula of Matsumani *et al.* [48] for an Fe target (1.70 atom/ion) and for an Al target (1.53 atom/ion) with normal incident 1 keV Ar^+ ions [77] would slightly favour preferential Fe sputtering and a surface enrichment in Al, as observed herein. Finally, the systematic return to the same $I_{Al\,2p}/I_{Fe\,3p}$ value (not shown) demonstrates that sputtering is efficient enough to remove the segregated layer between each experiment. For all orientations (Fig. 6), a clear enrichment of the surface in Al starts around 750 K. Since grazing measurements lead to higher composition values than for normal emission in the framework of a homogeneous bulk alloy model, a
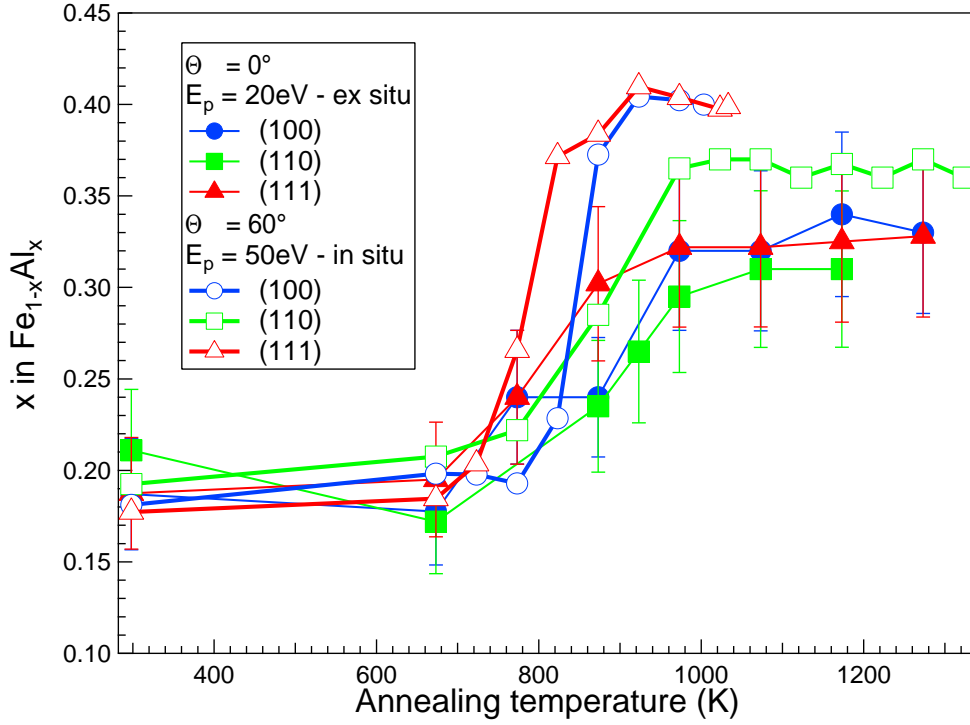
Figure 6: Comparison of Al segregation versus annealing temperature for $Fe_{0.85}Al_{0.15}(100)$, (110) and (111). The atomic fraction corresponds to an analysis of the $I_{Al\,2p}/I_{Fe\,3p}$ ratio using a homogeneous bulk material $Fe_{1-x}Al_x$. *Ex situ* data correspond to samples annealed directly after sputtering in the preparation chamber (normal emission) and *in situ* data to a progressive annealing on the analysis chamber manipulator (grazing emission $\Theta = 60°$). The analyzer pass energy E_p is different for the two sets of measurements.

16

segregation profile should exist with an enrichment of the extreme surface in Al compared to Fe. By comparing normal and grazing emission, the surface enrichment seems to be larger and quicker in temperature on the (100) and (111) than on the (110) surface and equilibration of the near surface is faster than bulk. Finally above ~ 950 K, the profile of segregation determined on the basis of photoemission data seems to reach a steady state.

In a second step, the variation of the photoelectron escape depth with emission angle Θ $(0 - 75°,$ Fig. 7) has been exploited to probe the segregation profile after annealing at 1273 K in the steady state regime (Fig. 6).

Model	Parameter	(100)	(110)	(111)
a) Film	Thickness t (Å)	24 ± 4	32 ± 7	23 ± 4
	Layer atomic fraction x_L	0.47 ± 0.02	0.4 ± 0.02	0.47 ± 0.03
b) Profile	Length Λ (Å)	26.6 ± 6	38 ± 10	25 ± 6
	Variation of atomic fraction Δx	0.35 ± 0.03	0.27 ± 0.02	0.35 ± 0.03
	Surface atomic fraction $x_s + \Delta x$	0.5 ± 0.03	0.42 ± 0.02	0.5 ± 0.03

Table 2: Results for the fit of the photoemission angular variation signal: a) with a segregated layer (Eq. 3, Fig. 5-c) or b) with a continuous segregation profile (Eq. 5, Fig. 5-d). The error bars stem from 10 % uncertainty on the corrected $I_{Al\,2p}/I_{Fe\,3p}$ ratio.

Fig. 7 shows a clear trend for all surfaces of Al enrichment near the extreme surface after an annealing at high temperature. The clear increase of the Al signal relative to Fe at grazing emission was fitted with either a homogeneous segregated layer (Fig. 5-b, Eq. 3) or a diffusion continuous profile (Fig. 5-c, Eq. 5). For both models, the substrate composition was kept fixed at the nominal value $x_S = 0.15$. Fits are shown as continuous lines in Fig. 7 and parameters are gathered in Tab. 2. Error bars on the fitted parameters $t, x_L, \Lambda, \Delta x$ stem from an uncertainty of 10 % on the corrected $I_{Al\,2p}/I_{Fe\,3p}$ ratio. As correlations between parameters do exist, it was checked that systematic errors due to the determination of the inelastic mean free paths from the TPP-2M formula (up to $\delta\lambda/\lambda \sim 20$ %) lead to fitted values of t or Λ that lie roughly within the same error bars (Tab. 2). In parallel, uncertainties in the atomic volume determination $V(x)$ come into play only to the second order; indeed as shown by Eq. 3, $V(x)$ appears only through a ratio:

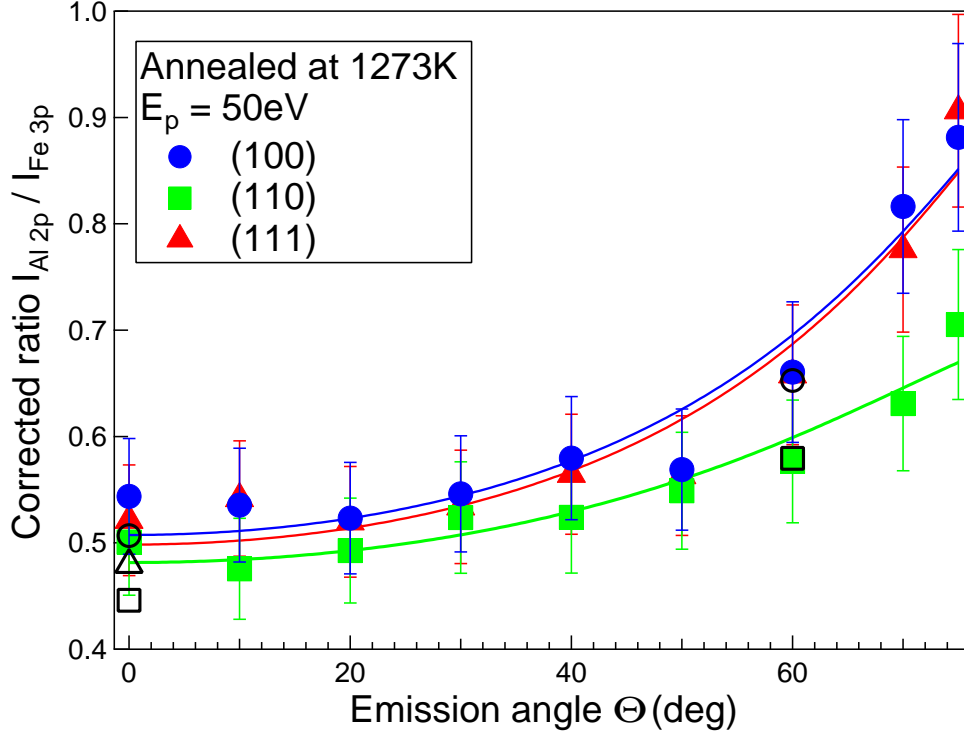$$\frac{V(x_L)}{V(x_S)} = \frac{V(x_L^0)}{V(x_S^0)} \tag{7}$$

Figure 7: Angular modulation of the $I_{Al\,2p}/I_{Fe\,3p}$ ratio (analyzer pass energy $E_p = 50$ eV) corrected from analyzer transmission function and photo-ionization cross-sections. Samples have been annealed at the highest temperature 1273 K corresponding to the segregation steady state regime. Data (points) have been fitted with a model of continuous segregation profile (lines, Eq. 5). Similar fit quality is obtained with the segregated layer model (Eq. 3). Black open symbols correspond to measurements at the highest temperature of Fig. 6.

$$\times \quad \left\{ 1 + \left[\left(\frac{\partial V}{\partial x} \right)_{x_L^0} - \left(\frac{\partial V}{\partial x} \right)_{x_S^0} \right] \delta x + O(\delta x^2) \right\},$$

in which the slopes at point x_L^0 and x_S^0 partially cancel out. Basically, the same argument holds for the λ-terms and also for Eq. 5. Therefore, x_L or Δx values are poorly influenced by systematic errors on inelastic mean free path or atomic volume.

While fits do not allow to favour one model over the other, both agree on the extreme surface composition and on the impacted depth which value justifies the above developed continuous approach despite the likely existence of more complex oscillatory segregation profiles. On (110) surfaces, the subsurface composition found over ~ 35 Å (~ 17 monolayers of (110) orientation) is close to $Fe_{0.6}Al_{0.4}$; it falls into the ordered B_2 range of stability according to the bulk phase diagram (Fig. 1). For (100) and (111), the composition $Fe_{0.53}Al_{0.47}$ is the Al-rich limit of the CsCl B_2 phase over a thickness of ~ 25 Å in both cases (~ 17 and ~ 30 monolayers, respectively, accounting for the spacing between (100) and (111) planes).

4. *Ab initio* calculations of Al segregation trends

Trends in Al segregation were estimated from energy differences between a single Al substitution (per surface unit cell) in the i-th atomic layer ($i = 1$ corresponds to the surface atomic layer) and in the slab center. Two types of surface unit cells have been used. The larger surface cells [(2×2) and (2×3)] enable in-plane Al-Al distances $d_{Al-Al} \geq 5.70$ Å, equal to or larger than these in the diluted bulk case $Fe_{0.9375}Al_{0.0625}$ (bcc). The smaller ones, (1×1), produce shorter in-plane Al-Al distances and enable to represent the atomic arrangement at surfaces of the $Fe_{0.5}Al_{0.5}$ (B_2) alloy.

Despite different Al densities in small and in large surface unit cells, the obtained segregation profiles at bare Fe surfaces (black and red lines in Fig. 8) show important similarities. Most of all, the well pronounced trend for surface segregation at all Fe termination is not affected by the precise configuration of Al atoms. Moreover, the energy differences between the two sets of configurations are systematically much smaller than the segregation energies themselves. The general oscillatory behaviour of E_{seg}^i for the three surfaces consists in a strong tendency for segregation at the surface (negative E_{seg}^i), followed by a sub-surface region in which segregation is not favoured
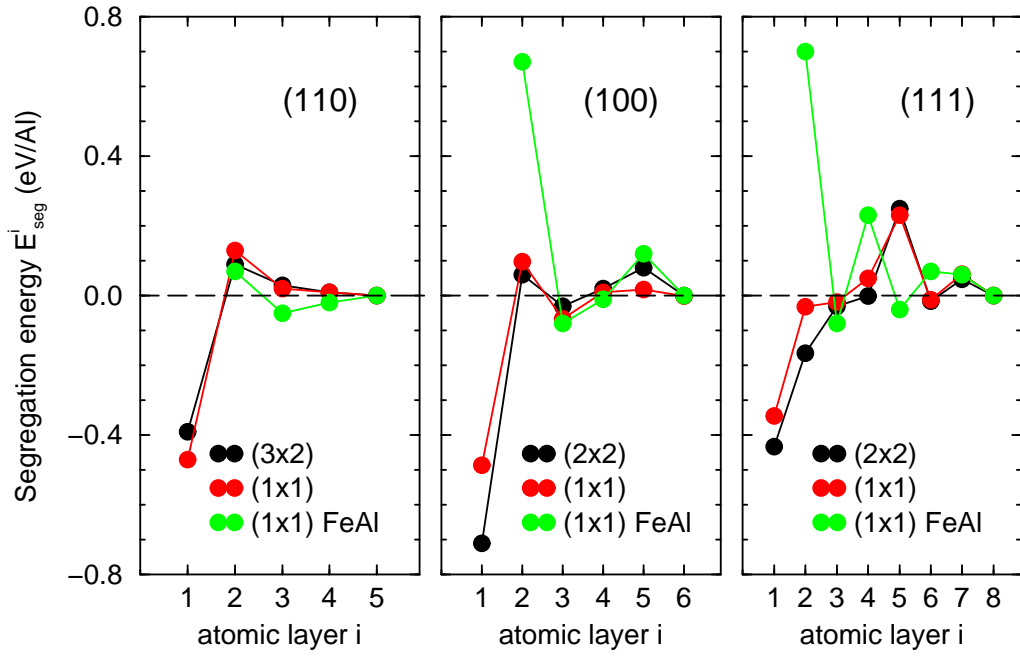
19

Figure 8: Layer-resolved segregation profiles energies of Al substitutions in Fe slabs of different orientations, bare (black and red lines) and FeAl-covered (green lines). Substitution energies in slab centers are used as references.

(positive E_{seg}^i). In the case of (110) and (100) surfaces both the surface and the subsurface regions consist essentially of Al enriched ($i = 1$) surface and a slightly depleted ($i = 2$) sub-surface, and variations of segregation profile are strongly attenuated already for $i \geq 3$. Conversely, in the case of the (111) orientation, the surface region with negative E_{seg}^i extends over three atomic layers ($i = 1 - 3$) and is followed by a Al-depleted sub-surface region composed of layers $i = 4$ and 5, the 5th one being particularly strongly unfavourable for Al segregation. In this case, variations of the segregation profile attenuate only below the 6th atomic layer. The large thickness of the (111) surface region is to be linked to the open character of the surface that involves under-coordinated atoms [atoms with missing nearest neighbours (NN)] down to the 2nd surface layer (4 NN and 7 NN in the 1st and 2nd surface layers, compared to 8 NN for bulk atoms). At the (110) and (100) surfaces instead, under-coordinated atoms are found in the 1st surface layer only (6 NN and 4 NN, respectively).

In the limit of low Al concentrations (large surface unit cells, black lines in Fig. 8), surface segregation is the most favoured at the (100) surface ($E_{seg}^1 \simeq -0.7$ eV). The (110) and (111) oriented surfaces are characterized by a similar E_{seg}^1 of about -0.4 eV. The main driving force responsible for such a stronger segregation at the (100) surface is the low coordination of its surface atoms. Indeed, if only NN interactions are taken into account, the segregation energy reads $E_{seg}^1 = Z'V + Z'(\epsilon_{Fe-Fe} - \epsilon_{Al-Al})/2$, with $2Z'$ being the number of out-of-plane bonds ($Z' = 2$, 4, and 4, for the (110), (100), and (111)-oriented atomic planes of the bcc lattice, respectively). The first term quantifies the energy loss due to broken surface mixed bonds. With $V = 0.2$ eV estimated from bulk calculations (see Sec. 2.5), it is systematically unfavorable to Al segregation (+0.4, +0.8, and +0.8 eV, respectively). The second term (-0.7, -1.4, and -1.4 eV, respectively) accounts for the difference of Fe and Al surface energies. Since those of Al are much lower, it is negative and strongly contributes towards surface segregation. The resulting estimation of E_{seg}^1 = -0.3, -0.6, and -0.6 eV, respectively, captures the essential difference of surface segregation at (110) and (100) surfaces. It is not sufficient to account for the particularity of the more open (111) termination, where substantial structural relaxations take place. More generally, the neglect of longer range interactions, of their dependence on the local environment and structural relaxations, makes the NN model qualitative and unable to account for the positive E_{seg} in the sub-surface region, and for the variation of E_{seg}^1 as a function of Al density.

The similarity of the segregation profiles at bare Fe surfaces obtained in large and small unit cells (black and red lines in Fig. 8), enables the estimation of the effect of a single surface FeAl layer (a single surface Al atom per (1×1) unit cell) on the segregation of subsequent Al, as to assess the possibility of formation of the FeAl alloy in the subsurface region. The computational results show that the presence of surface Al soundly modifies the Al segregation profiles (green lines) with respect to those obtained for bare Fe surfaces (red lines) and confers them a well pronounced oscillatory behaviour. Indeed, while the Al segregation to the sub-surface layer is systematically unfavourable ($E_{seg}^2 > 0$), $E_{seg}^3 \sim -0.1$ eV becomes negative for the three considered surfaces. We note, that the oscillations of E_{seg} at (100) and (111) surfaces mimic closely the composition of subsequent layers at the corresponding FeAl(100) and FeAl(111) surfaces. While similar, the effects are much less pronounced at the (110) surface. If estimated within the NN model, the unfavorable effect of Al atoms in the surface atomic layer, which is roughly proportional to the number of lost hetero-atomic bonds [+0.0, +1.6 and +0.9 eV for the (110), (100) and (111) surfaces, respectively] is indeed expected to be much smaller at the (110) surface. Also in this case, the neglect of longer range interactions and of the local environment effect makes the simple model only qualitative and unable to account for the subsequent oscillations of E_{seg}^i.

5. Discussion and conclusion

The composition of the sputtered $Fe_{0.85}Al_{0.15}$ surface was found close to the nominal one with a slight Al enrichment. Upon annealing of all the studied low index surfaces, photoemission evidences a strong aluminium segregation with a similar temperature onset around 700 K probably dictated by bulk diffusion [40]. Whatever the orientation, both photoemission analysis models (segregated film or profile) agree with a near surface composition close to $Fe_{0.5}Al_{0.5}$ with a typical affected depth of around 25 Å except on the (110) surface for which those figures are slightly different ($Fe_{0.6}Al_{0.4}$; ~ 35 Å; Tab. 2). Qualitatively in agreement with the existing literature obtained mainly on FeAl and with the calculated trends in surface segregation (Sect. 4), the thickness impacted by segregation is much larger than that determined previously by Auger spectroscopy or dynamic LEED measurements on FeAl [40, 38, 36, 41, 35, 37, 30, 25, 43, 36, 50]. It is also well

beyond the depth of the oscillatory behavior of composition found in the first layers of FeAl and predicted by the present calculations which additionally do not take into account entropic effects. According to the bulk phase diagram (Fig. 1), the profile of composition should cross all the transitions $A_2 \leftrightarrow D0_3 \leftrightarrow B_2$ from the bulk to the surface. Suspected in the diffraction experiment of Kottcke *et al.* [41] on FeAl(100) and in the Auger study of Hammer *et al.* [37] on the open FeAl(111) surface, such a gradient of composition was never really evidenced up to now in the $Fe_{1-x}Al_x$ system, probably because measurements focused on ordered Al-rich alloys. Stability of the B_2 and $D0_3$ phases with respect to the A_2 solid solution, might favor their formation at the surface of the alloy upon Al segregation. The observed segregation is likely a case of disordered (random) binary alloy in which short-range order plays a significant role in segregation with strong interactions between solute and solvent [29].

As much as the thickness of the segregated film found herein is in disagreement with the current description of the segregation at the FeAl alloy surfaces, it is reminiscent of the observed precipitation of B2 phases at the grain boundaries and shear planes of alloys mimicking low-density steels [4, 17, 18]. Such a segregation is likely to affect the macroscopic properties of a material, be it polycrystalline solid or formed of nanoparticles, as is often discussed [78]. In such context, $Fe_{0.85}Al_{0.15}$ random binary alloy crystal surfaces appear as quite relevant models.

6. Acknowledgements

References

[1] S. Deevi, V. Sikka, Nickel and iron aluminides: An overview on properties, processing, and applications, Intermetallics 4 (5) (1996) 357–375 (1996).

[2] D. G. Morris, M. A. Muñoz Morris, J. Chao, Development of high strength, high ductility and high creep resistant iron

aluminide, Intermetallics 12 (7) (2004) 821 – 826 (2004). doi:https://doi.org/10.1016/j.intermet.2004.02.032.
URL http://www.sciencedirect.com/science/article/pii/S0966979504000640

[3] M. Palm, Concepts derived from phase diagram studies for the strengthening of FeAl-based alloys, Intermetallics 13 (12) (2005) 1286 – 1295 (2005). doi:https://doi.org/10.1016/j.intermet.2004.10.015.
URL http://www.sciencedirect.com/science/article/pii/S0966979505000737

[4] S.-H. Kim, H. Kim, N. J. Kim, Brittle intermetallic compound makes ultrastrong low-density steel with large ductility, Nature 518 (2015) 77 (2015).
URL https://doi.org/10.1038/nature14144

[5] O. Grässel, L. Krüger, G. Frommeyer, L. W. Meyer, High strength Fe-Mn-(Al, Si) TRIP/TWIP steels development -properties-application, International Journal of Plasticity 16 (10) (2000) 1391 – 1409 (2000). doi:https://doi.org/10.1016/S0749-6419(00)00015-2.
URL http://www.sciencedirect.com/science/article/pii/S0749641900000152

[6] H. T. Jiang, W. Ding, D. Tand, W. Huang, Mechanical property and microstructural characterization of C-Mn-Al-Si hot dip galvanizing TRIP steel, Journal of Iron and Steel Research, International 19 (8) (2012) 29 – 36 (2012). doi:https://doi.org/10.1016/S1006-706X(12)60136-8.
URL http://www.sciencedirect.com/science/article/pii/S1006706X12601368

[7] I. Nikulin, T. Sawaguchi, K. Tsuzaki, Effect of alloying composition on low-cycle fatigue properties and microstructure of Fe-30Mn-(6-x)Si-xAl TRIP/TWIP alloys, Materials Science and Engineering: A 587 (2013) 192 – 200 (2013). doi:https://doi.org/10.1016/j.msea.2013.08.061.
URL http://www.sciencedirect.com/science/article/pii/S0921509313009489

[8] W. Wang, M. Li, C. He, X. Wei, D. Wang, H. Du, Experimental study on high strain rate behavior of high strength 600-1000MPa dual phase steels and 1200MPa fully martensitic steels, Materials & Design 47 (2013) 510 – 521 (2013). doi:https://doi.org/10.1016/j.matdes.2012.12.068.
URL http://www.sciencedirect.com/science/article/pii/S0261306912008977

[9] A. Mertens, E. M. Bellhouse, J. R. McDermid, Microstructure and mechanical properties of a mixed SiAl TRIP-assisted steel

subjected to continuous galvanizing heat treatments, Materials Science and Engineering: A 608 (2014) 249 – 257 (2014). doi:https://doi.org/10.1016/j.msea.2014.04.074.
URL http://www.sciencedirect.com/science/article/pii/S0921509314005371

[10] A. R. Marder, The metallurgy of zinc-coated steel, Prog. Mater Sci. 45 (3) (2000) 191 – 271 (2000). doi:https://doi.org/10.1016/S0079-6425(98)00006-1.
URL http://www.sciencedirect.com/science/article/pii/S0079642598000061

[11] P. Drillet, Z. Zermout, D. Bouleau, J. Mataigne, S. Claessens, Selective oxidation of high Si, Mn and Al steel grades during recrystallization annealing and steel/Zn reactivity, La Revue de Métallurgie-CIT 101 (10) (2004) 831–837 (2004).

[12] R. Cavallotti, J. Goniakowski, R. Lazzari, J. Jupille, A. Koltsov, D. Loison, Role of surface hydroxyl groups on zinc adsorption characteristics on $\alpha-\text{Al}_2\text{O}_3(0001)$ surfaces: first-principles study, J. Phys. Chem. C 118 (2014) 13578–13589 (2014).

[13] R. Cavallotti, Effets de la terminaison de l'α-alumine sur le comportement au mouillage du zinc, Ph.D. thesis, Pierre and Marie Curie University, France (2014).

[14] R. Cavallotti, H.-L. Thi Le, J. Goniakowski, R. Lazzari, J. Jupille, A. Koltsov, D. Loison, New routes for engineering the adhesion at $\text{Zn}/\alpha-\text{Al}_2\text{O}_3(0001)$ interface, Phys. Chem. Chem. Phys. 18 (2016) 3032–3039 (2016).

[15] H.-A. T. Le, J. Goniakowski, C. Noguera, A. Koltsov, J.-M. Mataigne, First-principles study on the effect of pure and oxidized transition-metal buffers on adhesion at the alumina/zinc interface, J. Phys. Chem. C 120 (2016) 9836–9844 (2016). doi:10.1021/acs.jpcc.6b02182.
URL http://dx.doi.org/10.1021/acs.jpcc.6b02182

[16] H.-L. Thi Le, R. Lazzari, J. Goniakowski, S. Cavallotti, R. Chenot, C. Noguera, J. Jupille, A. Koltsov, J.-M. Mataigne, Tuning adhesion at metal/oxide interfaces by surface hydroxylation, J. Phys. Chem. C 121 (2017) 11464–11471 (2017).

[17] S. Niu, H. Kou, T. Guo, Y. Zhang, J. Wang, J. Li, Strengthening of nanoprecipitations in an annealed $Al_{0.5}CoCrFeNi$ high entropy alloy, Materials Science and Engineering: A 671 (2016) 82–86 (2016). doi:https://doi.org/10.1016/j.msea.2016.06.040.

[18] X. Yang, F. P. Yuan, Q. G. Xie, Y. D. Wang, E. Ma, X. L. Wu, Strain hardening in Fe-16Mn-10Al-0.86C-5Ni high specific strength steel, Acta Materialia 109 (2016) 213–222 (2016). doi:https://doi.org/10.1016/j.actamat.2016.02.044.

[19] B. Predel, Al-Fe (Aluminum-Iron), in: Ac-Ag ... Au-Zr: Supplement to Subvolume IV/5A, Landolt-Börnstein-Group IV Physical Chemistry 12A: Physical Chemistry, Springer-Verlag Berlin Heidelberg, 2006, pp. 1–2 (2006).

[20] O. Kubaschewski, Iron binary phase diagrams, Springer Science & Business Media, 2013 (2013).

[21] V. Blum, On the interplay of surface segregation and bulk order in binary alloys : Structural investigations of iron and cobalt aluminium-based intermetallics, Ph.D. thesis, Erlangen-Nuremberg Univeristy (2001).

[22] Z. Liu, Y. Chang, Thermodynamic assessment of the Al-Fe-Si system, Metall. Mater. Trans. A 30 (4) (1999) 1081–1095 (1999).

[23] B. Sundman, I. Ohnuma, N. Dupin, U. R. Kattner, S. G. Fries, An assessment of the entire Al-Fe system including $d0_3$ ordering, Acta Materialia 57 (10) (2009) 2896–2908 (2009). doi:https://doi.org/10.1016/j.actamat.2009.02.046.

[24] A. T. Phan, M.-K. Paek, Y.-B. Kang, Phase equilibria and thermodynamics of the Fe-Al-C system: Critical evaluation, experiment and thermodynamic optimization, Acta Materialia 79 (2014) 1–5 (2014). doi:https://doi.org/10.1016/j.actamat.2014.07.006.

[25] V. Blum, L. Hammer, W. Meier, K. Heinz, M. Schmid, E. Lundgren, P. Varga, Segregation and ordering at $Fe_{1-x}Al_x$ (100) surfaces : a model case for binary alloys, Surf. Sci. 474 (1) (2001) 81–97 (2001).

[26] R. Rana, C. Liu, R. K. Ray, Low-density low-carbon feal ferritic steels, Scr. Mater. 68 (6) (2013) 354 – 359 (2013). doi:https://doi.org/10.1016/j.scriptamat.2012.10.004.

[27] U. Bardi, The atomic structure of alloy surfaces and surface alloys, Rep. Prog. Phys. 57 (10) (1994) 939–987 (1994).
URL http://stacks.iop.org/0034-4885/57/i=10/a=001

[28] M. Vasiliev, Surface effects of ordering in binary alloys, J. Phys. D 30 (22) (1997) 3037 (1997).
URL http://stacks.iop.org/0022-3727/30/i=22/a=002

[29] M. Polak, L. Rubinovich, The interplay of surface segregation and atomic order in alloys, Surf. Sci. Rep. 38 (4) (2000) 127–194 (2000).

[30] K. Heinz, L. Hammer, Surface structure and segregation of bimetallic bcc-type alloys, J. Phys.: Condens. Matter 11 (43) (1999) 8377 (1999).

[31] Y. Zhang, J. R. G. Evans, Z. S, Corrected values for boiling points and enthalpies of vaporization of elements in handbooks, J. Chem. Eng. Data. 56 (2011) 328–337 (2011).

[32] W. Tyson, W. Miller, Surface free energies of solid metals: Estimation from liquid surface tension measurements, Surf. Sci. 62 (1977) 267 (1977).

[33] H. Skriver, N. Rosengaard, Surface energy and work function of elemental metals, Phys. Rev. B 46 (1992) 7157–7168 (1992).

[34] L. Vitos, A. Ruban, H. Skriver, J. Kollár, The surface energy of metals, Surf. Sci. 411 (1998) 186 (1998).

[35] H. Graupner, L. Hammer, K. Müller, D. Zehner, Composition and structure of the (100) and (110) surfaces of FeAl, Surf. Sci. 322 (1995) 103–115 (1995).

[36] W. Meier, V. Blum, L. Hammer, K. Heinz, Equilibration of stoichiometrically distorted $Fe_{1-x}Al_x$ (100) surfaces, J. Phys.: Condens. Matter 13 (9) (2001) 1781–1791 (2001).

[37] L. Hammer, H. Graupner, V. Blum, K. Heinz, G. Ownby, D. Zehner, Segregation phenomena on surfaces of the ordered bimetallic alloy FeAl, Surf. Sci. 412-413 (1998) 69–81 (1998).

[38] B. Eltester, C. Uebing, H. Viefhaus, H. Grabke, AES and LEED investigation of Al segregation and oxidation of the (100) face of $Fe_{85}Al_{15}$ single crystals, Fresen. J. Anal. Chem. 358 (1-2) (1997) 196–199 (1997).

[39] O. Kizilkaya, D. Hite, D. Zehner, P. Sprunger, Surface reconstruction of FeAl(110) studied by scanning tunnelling microscopy and angle-resolved photoemission spectroscopy, J. Phys.: Condens. Matter 16 (30) (2004) 5395–5406 (Jul 2004). doi:10.1088/0953-8984/16/30/002.
URL http://dx.doi.org/10.1088/0953-8984/16/30/002

[40] M. Gemmaz, M. Afyouni, A. Mosser, Determination of the diffusion coefficient of Al in Fe-Al alloy by Auger spectrometry, Surf. Sci. Lett. 227 (1990) L109–L11 (1990).

[41] M. Kottcke, H. Graupner, D. Zehner, L. Hammer, K. Heinz, Segregation-induced subsurface restructuring of FeAl (100), Phys. Rev. B 54 (8) (1996) R5275 (1996).

[42] C. Wang, F. Jona, N. Gleason, D. Strongin, P. Marcus, Atomic structure of FeAl {001}, Surf. Sci. 298 (1) (1993) 114–120 (1993).

[43] V. Blum, L. Hammer, W. Meier, K. Heinz, Quantification of substitutional disorder and atomic vibrations by LEED-the role of parameter correlations, Surf. Sci. 488 (1) (2001) 219–232 (2001).

[44] A. Baddorf, S. Chandavarkar, Identification of an incommensurate $FeAl_2$ overlayer on FeAI(110) using x-ray diffraction and reflectivity, Physica B 221 (1996) 141–144 (1996).

[45] J. Pan, J. Ni, B. Yang, Stability of FeAl(110) alloy surface structures: a first principle study, Eur. Phys. J. B 73 (2010) 367–373 (2010).

[46] N. Gleason, D. Strongin, A photoelectron spectroscopy and thermal desorption study of CO on FeAl (110) and polycrystalline TiAl and NiAl, Surf. Sci. 295 (3) (1993) 306–318 (1993).

[47] N. Gleason, D. Strongin, Water adsorption and thermal decomposition on FeAl (110), J. Phys. Chem. 100 (48) (1996) 18829–18838 (1996).

[48] N. Matsunami, Y. Yamamura, Y. Itikawa, N. Itoh, Y. Kazumata, S. Miyagawa, K. Morita, R. Shimizu, H. Tawara, Energy dependence of the ion-induced sputtering yields of monatomic solids, At. Data Nucl. Data Tables 31 (1984) 1–80 (1984). doi:http://dx.doi.org/10.1016/0092-640X(84)90016-0.
URL http://www.sciencedirect.com/science/article/pii/0092640X84900160

[49] M. P. Seah, A quantitative framework for the analysis of surfaces by AES and XPS, Analysis 9 (5) (1981) 171–180 (1981).

[50] L. Hammer, W. Meier, V. Blum, K. Heinz, Equilibration processes in surfaces of the binary alloy Fe-Al, J. Phys: Condens. Matter 14 (2002) 4145–4164 (2002).

[51] M. Ellner, I. Park, On the partial atomic volume of aluminum in solid solutions based on the 3d transition metals and copper, Metallurgical and Materials Transactions A 33 (2002) 3591–3595 (2002).

[52] http://www.physik.de/mateck.

[53] Z. Dai, Orientation-dependent segregation and oxidation at $Fe_{0.85}Al_{0.15}$ random alloy surfaces, Ph.D. thesis, University Pierre et Marie Curie, France (2017).

[54] Z. Dai, P. Borghetti, Y. Mouchaal, S. Chenot, P. David, J. Jupille, G. Cabailh, R. Lazzari, Self-organized carbon-rich stripe formation from competitive carbon and aluminium segregation at $Fe_{0.85}Al_{0.15}(110)$ surfaces, Appl. Surf. Sci. 444 (2018) 457–466 (2018).

[55] S. Tanuma, C. J. Powell, D. R. Penn, Calculations of electron inelastic mean free paths: II Data for 27 elements over the 50-2000 eV range, Surf. Interface Anal. 17 (1991) 911–926 (1991).

[56] S. Tanuma, C. J. Powell, D. R. Penn, Calculations of electron inelastic mean free paths for 31 materials, Surf. Interface Anal. 11 (11) (1988) 577–589 (1988). doi:10.1002/sia.740111107.
URL http://dx.doi.org/10.1002/sia.740111107

[57] S. Tanuma, C. J. Powell, D. R. Penn, Calculations of electron inelastic mean free paths: III Data for 15 inorganic compounds over the 50-2000 eV range, Surf. Interface Anal. 17 (1991) 927–939 (1991).

[58] S. Tanuma, C. J. Powell, D. R. Penn, Calculations of electron inelastic mean free paths (IMFPS). IV. Evaluation of calculated IMFPs and of the predictive IMFP formula TPP-2 for electron energies between 50 and 2000 ev, Surf. Interface Anal. 20 (1) (1993) 77–89 (1993). doi:10.1002/sia.740200112.
URL http://dx.doi.org/10.1002/sia.740200112

[59] S. Tanuma, C. J. Powell, D. R. Penn, Calculations of electron inelastic mean free paths. V. Data for 14 organic compounds over the 50-2000 eV range, Surf. Interf. Anal. 21 (1994) 165–176 (1994).

[60] S. Tanuma, C. J. Powell, D. R. Penn, Calculations of electron inelastic mean free paths (IMFPs) VI. analysis of the Gries inelastic scattering model and predictive IMFP equation, Surf. Interface Anal. 25 (1) (1997) 25–35 (1997). doi:10.1002/(SICI)1096-9918(199701)25:1¡25::AID-SIA207¿3.0.CO;2-2.
URL http://dx.doi.org/10.1002/(SICI)1096-9918(199701)25:1<25::AID-SIA207>3.0.

[61] S. Tanuma, C. J. Powell, D. R. Penn, Calculation of electron inelastic mean free paths (IMFPs) VII. reliability of the TPP-2M IMFP predictive equation, Surf. Interface Anal. 35 (3) (2003) 268–275 (2003). doi:10.1002/sia.1526.
URL http://dx.doi.org/10.1002/sia.1526

[62] S. Tanuma, C. J. Powell, D. R. Penn, Calculations of electron inelastic mean free paths, Surf. Interface Anal. 37 (1) (2005) 1–14 (2005). doi:10.1002/sia.1997.
URL http://dx.doi.org/10.1002/sia.1997

[63] H. Shinotsuka, S. Tanuma, C. J. Powell, D. R. Penn, Calculations of electron inelastic mean free paths. X. Data for 41 elemental solids over the 50 eV to 200 keV range with the relativistic full Penn algorithm, Surf. Interface Anal. 47 (9) (2015) 871–888, sIA-15-0197 (2015). doi:10.1002/sia.5789.
URL http://dx.doi.org/10.1002/sia.5789

[64] S. Tougaard, QUASES-IMFP-TPP2M Software, http://www.quases.com/products/quases-imfp-tpp2m/.

[65] Inorganic crystal strcuture database, https://www.fiz-karlsruhe.de/de/leistungen/kristallographie/icsd.html.

[66] G. Kresse, J. Furthmüller, Efficient iterative schemes for *ab initio* total energy calculations using a plane-wave basis set, Phys. Rev. B 54 (1996) 11169–11186 (1996).

[67] G. Kresse, J. Hafner, *Ab initio* molecular dynamics for liquid metals, Phys. Rev. B 47 (1993) 558–561 (1993).

[68] P. E. Blöchl, Projector augmented-wave method, Phys. Rev. B 50 (1994) 17953–17979 (1994).

[69] G. Kresse, J. Joubert, From ultrasoft pseudopotentials to the projector augmented-wave method, Phys. Rev. B 59 (1999) 1758–1775 (1999).

[70] J. P. Perdew, J. A. Chevary, S. H. Vosko, K. A. Jackson, M. R. Pederson, D. J. Singh, C. Fiolhais, Atoms, molecules, solids, and surfaces: applications of the generalized gradient approximation for exchange and correlation, Phys. Rev. B 46 (1992) 6671–6687 (1992).

[71] R. Hultgren, P. Desai, D. Hawkins, M. Gleiser, K. Kelley, Selected values of the thermodynamic properties of binary alloys, Tech. rep., National Standard Reference Data System (1973).

[72] G. Das, B. Rao, P. Jena, S. Deevi, Electronic structure of substoichiometric Fe-Al intermetallics, Phys. Rev. B 66 (18) (2002) 184203 (2002).

[73] G. Tréglia, B. Legrand, F. Ducastelle, A. Saúl, c. Gallis, I. Meunier, C. Mottet, A. Senhaji, Alloy surfaces: segregation, reconstruction and phase transitions, Computational Materials Science 15 (1999) 196–235 (1999). doi:https://doi.org/10.1016/S0927-0256(99)00004-X.

[74] P. Ruffieux, P. Schwaller, O. Gröning, L. Schlapbach, P. Gröning, Q. C. Herd, D. Funnemann, J. Westermann, Experimental determination of the transmission factor for the Omicron EA125 electron analyzer, Rev. Sci. Instr. 71 (2000) 3634–3639 (2000).

[75] J. Yeh, I. Lindau, Atomic subshell photoionization cross sections and assymetry parameters: $1 \leq z \leq 300$, At. Data Nucl. Data Tables 32 (1985) 1–155 (1985).

[76] D. Shirley, High-resolution X-ray photoemission spectrum of valence bands of gold, Phys. Rev. B 5 (1972) 4709–4714 (1972).

[77] A simple sputter yield calculator, https://www.iap.tuwien.ac.at/www/surface/sputteryield.

[78] S.-M. Seo, H.-W. Jeong, Y.-K. Ahn, D. W. Yun, J.-H. Lee, Y.-S. Yoo, A comparative study of quantitative microsegregation analyses performed during the solidification of the Ni-base superalloy CMSX-10, Materials Characterization 89 (2014) 43–55 (2014). doi:https://doi.org/10.1016/j.matchar.2013.12.009.